Research Article | Vol. 32, No. 4 / 12 Feb 2024 / Optics Express 6494
Optics EXPRESS

Theory of four wave mixing-based parametric amplification of spin-orbit modes

HENRY F. ELDER,[1,2,3,*] SAI KANTH DACHA,[1,2,4] THOMAS E. MURPHY,[1,5] AND PHILLIP SPRANGLE[1,2,5]

[1]Institute for Research in Electronics and Applied Physics, University of Maryland, College Park, MD 20740, USA
[2]Department of Physics, University of Maryland, College Park, MD 20740, USA
[3]Naval Surface Warfare Center Carderock Division, West Bethesda, MD 20817, USA
[4]Department of Applied Physics and Applied Mathematics, Columbia University, New York, NY 10027, USA
[5]Department of Electrical & Computer Engineering, University of Maryland, College Park, MD 20740, USA
*helder@umd.edu

Abstract: We study the generation of spin-orbit (SO) modes via four-wave mixing (FWM)-based parametric amplification. SO modes carry quantized total angular momentum (TAM), and we show that FWM processes that generate new signals conserve TAM. This is a generalization of prior research which operated in a regime where FWM processes conserved spin and orbital angular momenta independently. We calculate the growth rates of new modes for both degenerate and nondegenerate pump configurations. Our theory is validated against numerical simulations for the cases where the generated signals are in the same SO mode(s) as the pump(s). We also calculate the growth rates of signals in SO modes other than the pumps.

1. Introduction

Light that carries orbital angular momentum (OAM), also referred to as optical vortices or twisted light, is characterized by a helical or twisted wavefront. In contrast to spin angular momentum (SAM), where photons are limited to two states, OAM allows for, in principle, an infinite set of spatially orthogonal states [1]. This feature makes OAM-carrying light a highly attractive platform for spatial division multiplexing and quantum key distribution in free space as well as guided-wave communication systems [2–4]. Vortex beams also have applications in particle trapping and optical tweezers [5], optical metrology [6], quantum optics [7,8], nanoscopy [9,10], and remote sensing [11,12].

For many of these applications, the ability to create light with a desired combination of SAM and OAM at specific frequencies and high powers is key. Generation and amplification of free space OAM beams, which are defined as having an azimuthally varying phase structure $\exp[i\ell\varphi]$ where ℓ and φ are the OAM topological charge and azimuthal coordinate respectively, has been explored using Raman amplification in plasma [13] and four-wave mixing (FWM) in ^{85}Rb atomic vapor [14]. In azimuthally symmetric fibers, high refractive index contrasts produce spin-orbit (SO) interactions. In simple terms, this refers to the dependence of the effective index of a fiber mode of a given OAM topological charge ℓ on its SAM [15,16]. Raman amplification of "SO modes" in fibers have been studied and demonstrated recently [17].

Of particular interest here is FWM-based parametric amplification of SO modes in fiber, for which a typical experimental configuration is provided in Fig. 1 [18,19]. High power SO modes are injected into a fiber that supports SO modes; one mode, labeled (+,+2), has a dominant left-circular polarization (LCP) component and OAM $\ell = +2$, while the other, labeled (–,+5), has a dominant right-circular polarization (RCP) component and OAM $\ell = +5$. Within the fiber, FWM processes can amplify an ambient noise field into Stokes and anti-Stokes pairs of new

#506984 https://doi.org/10.1364/OE.506984
Journal © 2024 Received 17 Oct 2023; revised 14 Jan 2024; accepted 23 Jan 2024; published 8 Feb 2024

Optics EXPRESS

SO modes. Conservation of energy dictates that the Stokes and anti-Stokes modes will have a symmetric detuning frequency Ω when the pumps have the same frequency, while conservation of linear and angular momentum will dictate which of the supported SO modes are excited. An optical spectrum analyzer, combined with bandpass filters and an SO mode imaging scheme, can fully characterize the fields produced in the fiber. We note that Raman scattering will also likely occur within the fiber, producing a broader Stokes-shifted peak which will be in a superposition of the pump SO modes [17,18].

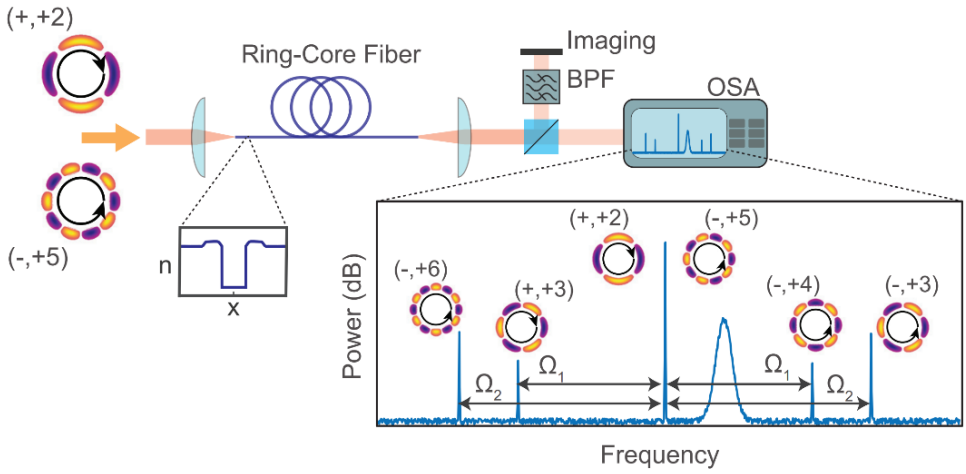

Fig. 1. A typical experimental setup and result of FWM-based parametric amplification of SO modes in fibers. The number of lobes in the field profiles indicate the OAM ℓ, while the circular arrow indicates the dominant polarization. BPF: band pass filter, OSA optical spectrum analyzer.

Although FWM-based parametric amplification has been described by applying the multimode nonlinear Schrödinger equations (MM-NLSEs) [18,20] to SO fiber modes, there remains a need for a more complete theoretical description of nonlinearly interacting SO modes that provides insight into how the angular momentum of light is transformed during the process. This is important not only for the aforementioned applications, but also in the context of the recent surge in interest in multimode nonlinear photonics [21–23]. In this work, we present, for the first time to our knowledge, a generalized theory of FWM-based parametric amplification of SO modes in azimuthally symmetric waveguides. We consider degenerate and nondegenerate pump cases for the spontaneous generation of new SO modes. We show that these processes conserve total angular momentum (TAM), but under certain conditions conserve SAM and OAM independently. We also compare our theory to numerical simulations for the cases where the generated Stokes and anti-Stokes signals are in the same SO modes as the pumps – equivalent to scalar modulation instability (SMI) and cross phase modulation instability (XPMI) of the pump beams.

This paper is organized as follows. First, we review the properties of SO modes in azimuthally symmetric waveguides. We then outline the derivation and results for the FWM-based parametric amplification processes and growth rates. These analytical results are compared to Fourier split-step simulations for the SMI and XPMI cases utilizing a fiber designed to accentuate SO interactions. Finally, we consider the generation of signals in SO modes different from the pump(s) by way of intermodal FWM.

Optics EXPRESS

2. Spin-orbit modes in azimuthally symmetric waveguides

Fibers with azimuthally symmetric refractive index profiles support modes $\mathbf{E}_q(\mathbf{r},t) = \tilde{\mathbf{F}}_q(\mathbf{r}_\perp,\omega_0)\exp[i(\beta_q(\omega_0)z-\omega_0 t)]$, where $\mathbf{E}_q(\mathbf{r},t)$ is the complex envelope of the electric field and $\tilde{\mathbf{F}}_q$ is the mode's electric field profile which has the form

$$\tilde{\mathbf{F}}_q(\mathbf{r}_\perp,\omega) = [\hat{\mathbf{r}}\,\tilde{F}_q^r(r,\omega) + \hat{\boldsymbol{\varphi}}\tilde{F}_q^\phi(r,\omega) + \hat{\mathbf{z}}\,\tilde{F}_q^z(r,\omega)]\exp[iJ\varphi]\,. \tag{1}$$

J denotes the total quantized angular momentum. Each photon in the mode carries $J\hbar$ angular momentum in the $\hat{\mathbf{z}}$ direction. An equivalent representation of $\tilde{\mathbf{F}}_q$ is produced by transforming to the circular polarization basis,

$$\begin{aligned}\tilde{\mathbf{F}}_q(\mathbf{r}_\perp,\omega) = {}& \hat{\boldsymbol{\sigma}}_+\,\tilde{F}_q^+(r,\omega)\exp[i(J-1)\varphi]\\ &+\hat{\boldsymbol{\sigma}}_-\,\tilde{F}_q^-(r,\omega)\exp[i(J+1)\varphi]\\ &+\hat{\mathbf{z}}\,\tilde{F}_q^z(r,\omega)\exp[iJ\varphi]\end{aligned} \tag{2}$$

where $\hat{\boldsymbol{\sigma}}_+ = \hat{\mathbf{x}} + i\hat{\mathbf{y}}$ denotes LCP and $\hat{\boldsymbol{\sigma}}_- = \hat{\mathbf{x}} - i\hat{\mathbf{y}}$ denotes RCP [24,25]. For typical step- and graded-index multimode fibers and air-core ring fibers, the transverse components of the mode profile are dominant. Transverse electric (TE) modes correspond to $J=0$, $\tilde{F}_q^- = -\tilde{F}_q^+$, and $\tilde{F}_q^z = 0$, and can be written as

$$\tilde{\mathbf{F}}_{(p,\mathrm{TE})}(\mathbf{r}_\perp,\omega) = \tilde{F}_{(p,\mathrm{TE})}^\perp(r,\omega)\,(\hat{\boldsymbol{\sigma}}_+\exp[-i\varphi] - \hat{\boldsymbol{\sigma}}_-\exp[i\varphi])\,, \tag{3}$$

where $\tilde{F}_{(p,\mathrm{TE})}^\perp = \tilde{F}_{(p,\mathrm{TE})}^+ = -\tilde{F}_{(p,\mathrm{TE})}^-$ and p is the radial order of the mode. That is, $\tilde{F}_{(p,\mathrm{TE})}^\perp$ has p zero-crossings in r. Similarly, transverse magnetic (TM) modes have $J=0$, $\tilde{F}_q^\perp = \tilde{F}_q^+ = \tilde{F}_q^-$, but $\tilde{F}_q^z \neq 0$, and take the form

$$\tilde{\mathbf{F}}_{(p,\mathrm{TM})}(\mathbf{r}_\perp,\omega) = \tilde{F}_{(p,\mathrm{TM})}^\perp(r,\omega)\,(\hat{\boldsymbol{\sigma}}_+\exp[-i\varphi] + \hat{\boldsymbol{\sigma}}_-\exp[i\varphi]) + \hat{\mathbf{z}}\,\tilde{F}_{(p,\mathrm{TM})}^z(r,\omega)\,. \tag{4}$$

Both TE and TM modes carry zero TAM. On the other hands, modes with $J \neq 0$ *do* carry a net TAM; in addition, one spin component will be dominant in the sense that, e.g., $\int d^2r\,|\tilde{F}_q^\pm|^2 > \int d^2r\,|\tilde{F}_q^\mp|^2$. It is common to express such spatial modes in terms of the OAM quanta ℓ carried by the dominant spin component rather than J, e.g. for a LCP-dominant mode

$$\begin{aligned}\tilde{\mathbf{F}}_{(p,+,\ell)}(\mathbf{r}_\perp,\omega) = {}& \hat{\boldsymbol{\sigma}}_+\,\tilde{F}_{(p,+,\ell)}^+(r,\omega)\,\exp[i\ell\varphi]\\ &+\hat{\boldsymbol{\sigma}}_-\,\tilde{F}_{(p,+,\ell)}^-(r,\omega)\,\exp[i(\ell+2)\varphi]\\ &+\hat{\mathbf{z}}\,\tilde{F}_{(p,+,\ell)}^z(r,\omega)\,\exp[i(\ell+1)\varphi],\end{aligned} \tag{5}$$

where $\ell = J-1$. Similarly, for a RCP-dominant mode,

$$\begin{aligned}\tilde{\mathbf{F}}_{(p,-,\ell)}(\mathbf{r}_\perp,\omega) = {}& \hat{\boldsymbol{\sigma}}_+\,\tilde{F}_{(p,-,\ell)}^+(r,\omega)\,\exp[i(\ell-2)\varphi]\\ &+\hat{\boldsymbol{\sigma}}_-\,\tilde{F}_{(p,-,\ell)}^-(r,\omega)\,\exp[i\ell\varphi]\\ &+\hat{\mathbf{z}}\,\tilde{F}_{(p,-,\ell)}^z(r,\omega)\,\exp[i(\ell-1)\varphi],\end{aligned} \tag{6}$$

where $\ell = J+1$. In either case, the TAM for the $(p,\pm,\ell)$ mode can be recovered via $J = s+\ell$, where $s = +1$ for LCP-dominant modes and $s = -1$ for RCP-dominant modes. Depending on the design of the waveguide and the values of ℓ under consideration, the "recessive" spin and longitudinal components of the modes may be sufficiently small such that the approximate representation $\tilde{\mathbf{F}}_{(p,\pm,\ell)}(\mathbf{r}_\perp,\omega) \simeq \hat{\boldsymbol{\sigma}}_\pm F_{(p,\pm,\ell)}(r,\omega)\exp[i\ell\varphi]$ is well justified. However, this is not generally valid, and there are important ramifications regarding selection rules for FWM processes that we will consider.

Optics EXPRESS

3. Four wave mixing of spin-orbit modes: theory

We now consider how SO modes interact in FWM processes. The derivation for the governing equations is based on the generalized multimode nonlinear Schrödinger equation (MMNLSE) as described in Refs [26,27]. We consider the electric and magnetic fields inside the fiber as the sum of spatial modes q, each at a frequency ω_q which are in the vicinity of a common carrier frequency ω_0,

$$\begin{aligned}\mathbf{E}(\mathbf{r},t) &= \sum_q A_q(z)\tfrac{\tilde{\mathbf{F}}_q(\mathbf{r}_\perp,\omega_0)}{N_q(\omega_0)}\exp[i(\beta_q(\omega_q)z-\omega_q t)]\,,\\ \mathbf{H}(\mathbf{r},t) &= \sum_q A_q(z)\tfrac{\tilde{\mathbf{G}}_q(\mathbf{r}_\perp,\omega_0)}{N_q(\omega_0)}\exp[i(\beta_q(\omega_q)z-\omega_q t)]\,,\end{aligned} \tag{7}$$

where $|\omega_0-\omega_q|\ll\omega_0$, $\omega_q>0$, A_q is the longitudinal envelope, $\tilde{\mathbf{F}}_q$ and $\tilde{\mathbf{G}}_q$ are the mode profiles (approximated by their value at ω_0 rather than ω_q), β_q is the propagation constant, and N_q is a normalization (and mode orthogonality condition) given by

$$\delta_{q,q'}N_q^2(\omega_0)=\frac{1}{4}\int d^2r\;\hat{\mathbf{z}}\cdot(\tilde{\mathbf{F}}_q(\mathbf{r},\omega_0)\times\tilde{\mathbf{G}}^*_{q'}(\mathbf{r},\omega_0)-\tilde{\mathbf{G}}_q(\mathbf{r},\omega_0)\times\tilde{\mathbf{F}}^*_{q'}(\mathbf{r},\omega_0))\,. \tag{8}$$

Note that, by requiring the envelopes to have the form $A_q(z)$, we are assuming continuous wave (CW) signals; we will lift this assumption later in the paper to allow for temporal variations in the envelopes. Proceeding with the derivation of the MMNLSE, we arrive at

$$\partial_z A_q(z)=\frac{-1}{4N_q(\omega_0)}\exp[-i(\beta_q(\omega_q)z-\omega_q t)]\int d^2r\;\tilde{\mathbf{F}}^*_q(\omega_0)\cdot\partial_t\mathbf{P}_{\rm NL}(\mathbf{r},t)\,. \tag{9}$$

In this work, we are concerned with FWM processes driven by the instantaneous third-order nonlinear susceptibility. Thus the nonlinear polarization $\mathbf{P}_{\rm NL}$ is given by

$$\mathbf{P}_{\rm NL}=\frac{\varepsilon_0\chi^{(3)}}{4}[2|\mathbf{E}|^2\mathbf{E}+(\mathbf{E}\cdot\mathbf{E})\mathbf{E}^*]\exp[-i\omega_0 t]\,, \tag{10}$$

where we have set $\chi^{(3)}=\chi^{(3)}_{xxxx}$ and discarded the third harmonic term. Consider the case where the fields are composed of two pumps, labeled as modes 1 and 2, and an arbitrary collection of smaller amplitude signals S, i.e.

$$\begin{aligned}\mathbf{E}(\mathbf{r},\mathbf{t}) &= A_1(z)\tfrac{\tilde{\mathbf{F}}_1(\mathbf{r}_\perp,\omega_0)}{N_1(\omega_0)}\exp[i(\beta_1(\omega_1)z-\omega_1 t)]\\ &+A_2(z)\tfrac{\tilde{\mathbf{F}}_2(\mathbf{r}_\perp,\omega_0)}{N_2(\omega_0)}\exp[i(\beta_2(\omega_2)z-\omega_2 t)]\\ &+\sum_{\rm S}A_{\rm S}(z)\tfrac{\tilde{\mathbf{F}}_{\rm S}(\mathbf{r}_\perp,\omega_0)}{N_{\rm S}(\omega_0)}\exp[i(\beta_{\rm S}(\omega_{\rm S})z-\omega_{\rm S}t)]\,.\end{aligned} \tag{11}$$

Combining Eqs. (9)–(11) and assuming $\beta_1(\omega_1)\neq\beta_2(\omega_2)$, the governing equations for the pumps are given by

$$\begin{aligned}\partial_z A_1(z) &= i\alpha_1[Q_1^{(\rm SPM)}|A_1|^2+Q_{1,2}^{(\rm XPM)}|A_2|^2]A_1\,,\\ \partial_z A_2(z) &= i\alpha_2[Q_{2,1}^{(\rm XPM)}|A_1|^2+Q_2^{(\rm SPM)}|A_2|^2]A_2\,.\end{aligned} \tag{12}$$

where $\alpha_q=\varepsilon_0\,\chi^{(3)}\,\omega_q\,/\,8$ and the Q terms are overlap integrals for self-phase modulation (SPM) and cross-phase modulation (XPM) processes,

$$\begin{aligned}Q_q^{(\rm SPM)} &= \tfrac{1}{N_q^4}\int d^2r\;\left[|\tilde{\mathbf{F}}_q|^4+\tfrac{1}{2}(\tilde{\mathbf{F}}_q\cdot\tilde{\mathbf{F}}_q)(\tilde{\mathbf{F}}^*_q\cdot\tilde{\mathbf{F}}^*_q)\right],\\ Q_{q,j}^{(\rm XPM)} &= \tfrac{1}{N_q^2N_j^2}\int d^2r\;[|\tilde{\mathbf{F}}_q|^2|\tilde{\mathbf{F}}_j|^2+(\tilde{\mathbf{F}}_q\cdot\tilde{\mathbf{F}}_j)(\tilde{\mathbf{F}}^*_q\cdot\tilde{\mathbf{F}}^*_j)+(\tilde{\mathbf{F}}^*_q\cdot\tilde{\mathbf{F}}_j)(\tilde{\mathbf{F}}_q\cdot\tilde{\mathbf{F}}^*_j)]\,.\end{aligned} \tag{13}$$

Since $Q_q^{(\rm SPM)}$ and $Q_{q,j}^{(\rm XPM)}$ are real-valued, $|A_1(z)|^2$ and $|A_2(z)|^2$ are z-invariant and Eqs. (12) can be solved directly even though they form a coupled nonlinear system. The equation for an

Optics EXPRESS

arbitrary signal S will include cross phase modulation by the two pumps and numerous other nonlinear terms. If we only consider signals that can undergo amplification, even from noise, one obtains

$$\begin{aligned}\partial_z A_{\rm S}(z) = i\alpha_{\rm S}[&(Q_{\rm S,1}^{\rm (XPM)}|A_1|^2 + Q_{\rm S,2}^{\rm (XPM)}|A_2|^2)A_{\rm S} \\ &+\sum_{\rm A} Q_{\rm S,A}^{\rm (FWM1)} A_1^2 A_{\rm A}^* \exp[i\,(2\beta_1 - \beta_{\rm A} - \beta_{\rm S})z]\ \delta(2\omega_1 - \omega_{\rm A} - \omega_{\rm S}) \\ &+Q_{\rm S,A}^{\rm (FWM2)} A_2^2 A_{\rm A}^* \exp[i\,(2\beta_2 - \beta_{\rm A} - \beta_{\rm S})z]\,\delta(2\omega_2 - \omega_{\rm A} - \omega_{\rm S}) \\ &+Q_{\rm S,A}^{\rm (FWM3)} A_1 A_2 A_{\rm A}^* \exp[i\,(\beta_1 + \beta_2 - \beta_{\rm A} - \beta_{\rm S})z]\,\delta(\omega_1 + \omega_2 - \omega_{\rm A} - \omega_{\rm S})]\,,\end{aligned} \tag{14}$$

where mode A is another mode generated along with mode S, and the overlap integrals for the different FWM processes are given by

$$\begin{aligned}Q_{\rm S,A}^{\rm (FWM1)} &= \tfrac{1}{N_1^2 N_{\rm S} N_{\rm A}} \int d^2r\ \left[(\tilde{\mathbf{F}}_1\cdot\tilde{\mathbf{F}}_{\rm S}^*)(\tilde{\mathbf{F}}_1\cdot\tilde{\mathbf{F}}_{\rm A}^*) + \tfrac{1}{2}(\tilde{\mathbf{F}}_1\cdot\tilde{\mathbf{F}}_1)(\tilde{\mathbf{F}}_{\rm S}^*\cdot\tilde{\mathbf{F}}_{\rm A}^*)\right], \\ Q_{\rm S,A}^{\rm (FWM2)} &= \tfrac{1}{N_2^2 N_{\rm S} N_{\rm A}} \int d^2r\ \left[(\tilde{\mathbf{F}}_2\cdot\tilde{\mathbf{F}}_{\rm S}^*)(\tilde{\mathbf{F}}_2\cdot\tilde{\mathbf{F}}_{\rm A}^*) + \tfrac{1}{2}(\tilde{\mathbf{F}}_2\cdot\tilde{\mathbf{F}}_2)(\tilde{\mathbf{F}}_{\rm S}^*\cdot\tilde{\mathbf{F}}_{\rm A}^*)\right], \\ Q_{\rm S,A}^{\rm (FWM3)} &= \tfrac{1}{N_1 N_2 N_{\rm S} N_{\rm A}} \int d^2r\,[(\tilde{\mathbf{F}}_1\cdot\tilde{\mathbf{F}}_{\rm S}^*)(\tilde{\mathbf{F}}_2\cdot\tilde{\mathbf{F}}_{\rm A}^*) + (\tilde{\mathbf{F}}_2\cdot\tilde{\mathbf{F}}_{\rm S}^*)(\tilde{\mathbf{F}}_1\cdot\tilde{\mathbf{F}}_{\rm A}^*) \\ &\quad +(\tilde{\mathbf{F}}_1\cdot\tilde{\mathbf{F}}_2)(\tilde{\mathbf{F}}_{\rm S}^*\cdot\tilde{\mathbf{F}}_{\rm A}^*)]\,.\end{aligned} \tag{15}$$

With $\omega_{\rm S} < \omega_{\rm A}$, S can naturally be identified as the Stokes mode and A the anti-Stokes. The governing equation for mode A is obtained by the substitution S $\leftrightarrow$ A. In addition, we can identify FWM1(2) as corresponding to *degenerate* FWM from pump 1(2), and FWM3 to *nondegenerate* FWM.

Angular momentum selection rules, embedded within the overlap integrals Q, dictate which SO modes interact with each other via FWM. Considering the forms of the spatial modes provided in Eq. (1), the azimuthal integration for $Q_{\rm S,A}^{\rm (FWM1)}$ is nonzero only if $2J_1 = J_{\rm S} + J_{\rm A}$. Similarly, $Q_{\rm S,A}^{\rm (FWM2)}$ requires $2J_2 = J_{\rm S} + J_{\rm A}$, and $Q_{\rm S,A}^{\rm (FWM3)}$ requires $J_1 + J_2 = J_{\rm S} + J_{\rm A}$. Thus, since J determines the TAM of the mode, one can say the TAM of the light is conserved during the FWM processes. When the modes involved in a particular FWM process carry nonzero TAM and have negligibly small recessive spin components such that the approximate form $\tilde{\mathbf{F}}_{(p,\pm,\ell)}(\mathbf{r}_\perp,\omega_0) \simeq \hat{\boldsymbol{\sigma}}_\pm \tilde{F}_{(p,\pm,\ell)}(r,\omega_0)\exp[i\ell\varphi]$ is accurate, the overlap integrals are nonzero only when OAM and SAM are conserved independently. For example, in this regime, $Q^{\rm (FWM3)} \neq 0$ only when $\ell_1 + \ell_2 = \ell_{\rm S} + \ell_{\rm A}$ and $s_1 + s_2 = s_{\rm S} + s_{\rm A}$, where $s = +1$ for LCP-dominant modes and $s = -1$ for RCP-dominant modes. This latter case was observed experimentally in Ref. [18].

Assuming the frequency matching conditions (delta functions in Eq. (14)) are satisfied, and that the pumps carry undepleted powers P_1 and P_2, one can show that each FWM term can lead to the growth of new SO modes. The resultant growth rates for each FWM process are

$$\begin{aligned}g^{\rm (FWM1)} &= \sqrt{4\alpha_{\rm S}\alpha_{\rm A}\, Q_{\rm S,A}^{\rm (FWM1)^2} P_1^2 - \kappa^{\rm (FWM1)2}}\,, \\ \kappa^{\rm (FWM1)} &= 2\beta_1(\omega_1) - \beta_{\rm S}(\omega_{\rm S}) - \beta_{\rm A}(\omega_{\rm A}) + 2\theta_1 - \theta_{\rm S} - \theta_{\rm A}\,,\end{aligned} \tag{16}$$

$$\begin{aligned}g^{\rm (FWM2)} &= \sqrt{4\alpha_{\rm S}\alpha_{\rm A}\, Q_{\rm S,A}^{\rm (FWM2)^2} P_2^2 - \kappa^{\rm (FWM2)2}}\,, \\ \kappa^{\rm (FWM2)} &= 2\beta_2(\omega_2) - \beta_{\rm S}(\omega_{\rm S}) - \beta_{\rm A}(\omega_{\rm A}) + 2\theta_2 - \theta_{\rm S} - \theta_{\rm A}\,,\end{aligned} \tag{17}$$

$$\begin{aligned}g^{\rm (FWM3)} &= \sqrt{4\alpha_{\rm S}\alpha_{\rm A}\, Q_{\rm S,A}^{\rm (FWM3)^2} P_1 P_2 - \kappa^{\rm (FWM3)2}}\,, \\ \kappa^{\rm (FWM3)} &= \beta_1(\omega_1) + \beta_2(\omega_2) - \beta_{\rm S}(\omega_{\rm S}) - \beta_{\rm A}(\omega_{\rm A}) + \theta_1 + \theta_2 - \theta_{\rm S} - \theta_{\rm A}\,,\end{aligned} \tag{18}$$

Optics EXPRESS

where each θ is a nonlinear phase shift

$$\begin{aligned}\theta_1 &= \alpha_1(Q_1^{(\mathrm{SPM})}P_1 + Q_{1,2}^{(\mathrm{XPM})}P_2),\\ \theta_2 &= \alpha_2(Q_{2,1}^{(\mathrm{XPM})}P_1 + Q_2^{(\mathrm{SPM})}P_2),\\ \theta_\mathrm{S} &= \alpha_\mathrm{S}(Q_{\mathrm{S},1}^{(\mathrm{XPM})}P_1 + Q_{\mathrm{S},2}^{(\mathrm{XPM})}P_2),\\ \theta_\mathrm{A} &= \alpha_\mathrm{A}(Q_{\mathrm{A},1}^{(\mathrm{XPM})}P_1 + Q_{\mathrm{A},2}^{(\mathrm{XPM})}P_2).\end{aligned} \tag{19}$$

A Stokes and anti-Stokes mode pair will stably grow when g is real-valued. The growth rate is maximized under the phase matching condition $\kappa = 0$, and larger pump powers will increase the bandwidth over which the modes will grow. For SO modes, additional mode selectivity is achieved by the constraint of conservation of TAM. Note that the growth rates in Eqs. (16)–(18) are the power e-folding lengths, e.g. $P_\mathrm{S}(z)$=$P_\mathrm{S}(0)\exp[gz]$.

4. Simulation overview and fiber description

Directly solving Eqs. (12) and (14) would require construction of a $N_m \times N_\omega$ system of equations, where N_m is the number of modes and N_ω the number of discrete frequency bins. One can reduce this to a N_m system by allowing the mode envelopes to have a time dependence, i.e. $A_q(z) \rightarrow A_q(z,t)$. Doing so and rederiving Eqs. (12) and (14) yields

$$\begin{aligned}\partial_z A_1(z,t) &= \left[\sum_{k>0} \tfrac{i^{k+1}}{k!}\beta_{k,1}\partial_t^k + i\alpha_1(Q_1^{(\mathrm{SPM})}|A_1|^2 + Q_{1,2}^{(\mathrm{XPM})}|A_2|^2)\right]A_1,\\ \partial_z A_2(z,t) &= \left[\sum_{k>0} \tfrac{i^{k+1}}{k!}\beta_{k,2}\partial_t^k + i\alpha_2(Q_{2,1}^{(\mathrm{XPM})}|A_1|^2 + Q_2^{(\mathrm{SPM})}|A_2|^2)\right]A_2,\end{aligned} \tag{20}$$

$$\begin{aligned}\partial_z A_\mathrm{S}(z,t) = &\left[\sum_{k>0} \tfrac{i^{k+1}}{k!}\beta_{k,\mathrm{S}}\partial_t^k + i\alpha_\mathrm{S}(Q_{\mathrm{S},1}^{(\mathrm{XPM})}|A_1|^2 + Q_{\mathrm{S},2}^{(\mathrm{XPM})}|A_2|^2)\right]A_\mathrm{S}\\ &+i\alpha_\mathrm{S}\left[\sum_\mathrm{A} Q_{\mathrm{S,A}}^{(\mathrm{FWM1})}A_1^2A_\mathrm{A}^*\exp\{i[(2\beta_1-\beta_\mathrm{A}-\beta_\mathrm{S})z-(2\omega_1-\omega_\mathrm{A}-\omega_\mathrm{S})t]\}\right.\\ &+Q_{\mathrm{S,A}}^{(\mathrm{FWM2})}A_2^2A_\mathrm{A}^*\exp\{[(2\beta_2-\beta_\mathrm{A}-\beta_\mathrm{S})z-(2\omega_2-\omega_\mathrm{A}-\omega_\mathrm{S})t]\}\\ &\left.+Q_{\mathrm{S,A}}^{(\mathrm{FWM3})}A_1A_2A_\mathrm{A}^*\exp\{i[(\beta_1+\beta_2-\beta_\mathrm{A}-\beta_\mathrm{S})z-(\omega_1+\omega_2-\omega_\mathrm{A}-\omega_\mathrm{S})t]\}\right],\end{aligned} \tag{21}$$

where $\beta_{k,q}(\omega_0) = (\partial^k\beta_q(\omega)/\partial\omega^k)_{\omega_0}$ accounts for dispersion. The number of terms required in the dispersion expansion will depend on the bandwidth under consideration. The dynamics equation for the anti-Stokes mode A is obtained by the substitution S $\leftrightarrow$ A in Eq. (21). While Eqs. (20) are in a form which can be solved using the nonlinear Fourier split-step technique [28], Eq. (21) requires a much slower finite-difference procedure. In addition, the nature of Eq. (21) necessitates an extremely small z step size to accurately capture potentially high frequency oscillations. As such, in this portion of the paper we limit our efforts to utilizing Eq. (20) to perform a partial validation of our analysis. That is, we explore FWM-based parametric amplification where the generated Stokes and anti-Stokes signals are both in the same spatial mode(s) as the pump(s), but at new frequencies. In this case the FWM processes are equivalent to the scalar modulation instability (SMI) and cross-phase modulation instability (XPMI) previously explored in both single-mode and multi-mode fibers [29,30].

Since the Fourier split-step simulation technique requires a finite-duration pulse, we use a $T = 0.8$ ns length supergaussian pulse, i.e. $A_q(z=0,t) \propto \exp[-(2t/T)^{16}]$. For each test case we perform 100 simulations with white Gaussian noise added to the beam profiles before propagation. This acts as a seed for signal generation. We then analyze the ensemble average spectra after propagation. When performing the Fourier transforms of the final envelopes, we only utilize the

Optics EXPRESS

beam content within the pulse width to better approximate CW behavior. Dispersion terms up to fourth order (β_4) are included to ensure that the phase matching processes within the simulations are accurate across the bandwidth of interest.

As for the fiber, we consider an air-core ring fiber as shown in Fig. 2(a) [15–19,24]. It consists of an 8 µm radius air-filled core surrounded by a 2 µm thick high refractive index ring of a GeO_2-SiO_2 mixture, followed by a cladding of pure SiO_2. The ring-shaped refractive index profile allows for the stable guiding of SO modes which have characteristic donut intensity profiles. Examples of mode profiles are shown in Fig. 2(b). We observe that, for the (0,+,–2) mode, the recessive spin component (RCP in this case) is comparable to, but still smaller than, the dominant spin component (LCP). On the other hand, the higher-ℓ mode (0,+,+8) has a fairly negligible recessive spin component. To characterize this effect across all modes in the fiber, we quantify the relative strengths of each mode's $\hat{\mathbf{e}}_j = \{\hat{\boldsymbol{\sigma}}_+, \hat{\boldsymbol{\sigma}}_-, \hat{\mathbf{z}}\}$ component as

$$\bar{P}_q^j = \frac{\int d^2r \, |\tilde{\mathbf{F}}_q(\mathbf{r}_\perp, \omega_0) \cdot \hat{\mathbf{e}}_j|^2}{\int d^2r \, |\tilde{\mathbf{F}}_q(r_\perp, \omega_0)|^2} \, . \tag{22}$$

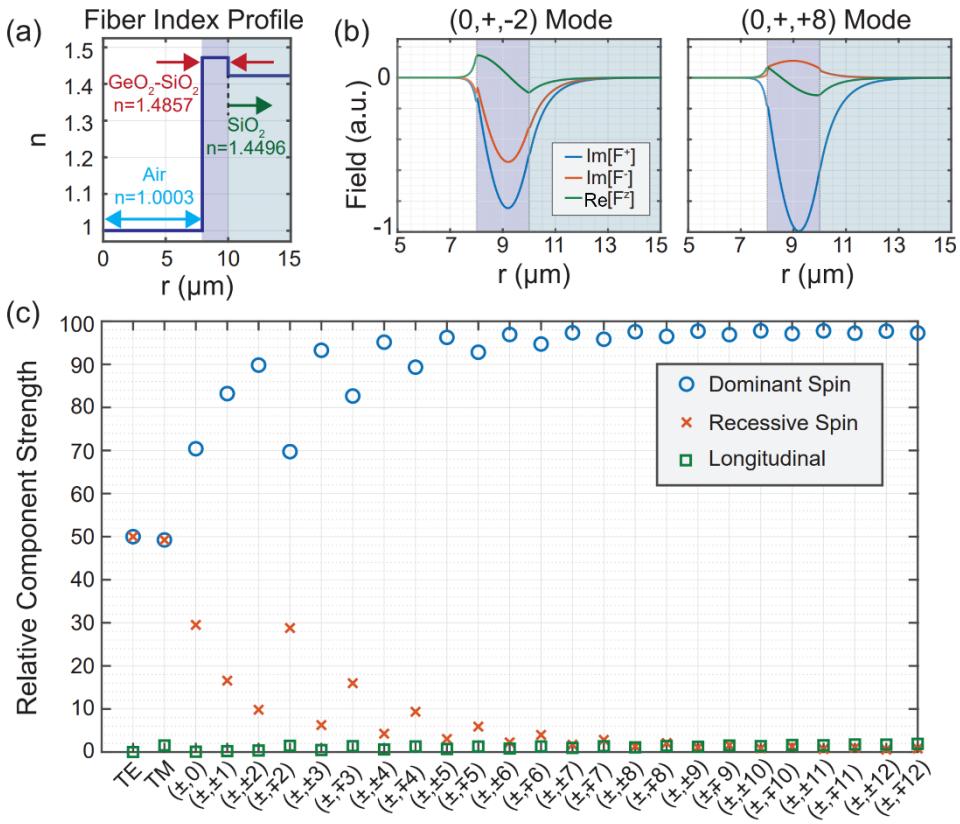

Fig. 2. (a) Refractive index profile for the air-core ring fiber under consideration. (b) Field profiles of the (0,+,–2) and (0,+,+8) modes. The mode solving procedure utilized generates profiles with purely real longitudinal components and purely complex LCP and RCP components. (c) Relative strengths of mode components for select fiber modes, quantified per Eq. (22). The radial orders p is omitted to keep the figure more legible but are equal to 0. All quantities displayed are evaluated at 1.064 µm.

Optics EXPRESS

The results for a selection of modes are shown in Fig. 2(c). As discussed earlier, the two spin components for TE and TM modes have the same strengths. Additionally, as ℓ increases, the recessive spin component does become weak. Generally speaking, modes with higher ℓ can be well approximated by the profile $\tilde{\mathbf{F}}_{(p,\pm,\ell)}(\mathbf{r}_\perp,\omega_0)\simeq\hat{\boldsymbol{\sigma}}_\pm\tilde{F}_{(p,\pm,\ell)}(r,\omega_0)\exp[i\ell\varphi]$, and FWM processes amongst these modes will, also to good approximation, conserve OAM and SAM independently. On the other hand, TE, TM, and modes with low ℓ are better described by their full forms Eqs. (3)–(6), and will not have such a restriction. What quantifies as "high" versus "low" ℓ will vary depending on the fiber design and the level of analytical precision desired.

Further details on the fiber design and its modal properties are presented in the Supplement 1.

5. Scalar modulation instability of the (0,–,+8) mode

We first explore the case of a single pump: a 0.8 ns supergaussian pulse in the (0,–,+8) spatial mode at 1.064 µm, with 1 kW peak power propagating over 3 meters. We consider only new Stokes and anti-Stokes signals which are also in the (0,–,+8) spatial mode; this is equivalent to scalar modulation instability (SMI). The relevant dispersion and overlap coefficients are provided in the first column of Table 1. Note that, for SMI, $Q^{(\mathrm{SPM})}=Q^{(\mathrm{FWM1})}$. Since this mode is in the anomalous dispersion regime it will undergo the typical scalar modulation instability and develop broad, symmetric sidebands about the pump frequency with peaks at $\lambda_S=1.108$ µm and $\lambda_A=1.023$ µm. In addition, the dispersion curve is phase matched at a further detuning with peaks at $\lambda_S=1.305$ µm, $\lambda_A=0.898$ µm. The simulation results are compared to the predictions of Eq. (16) in Fig. (3).

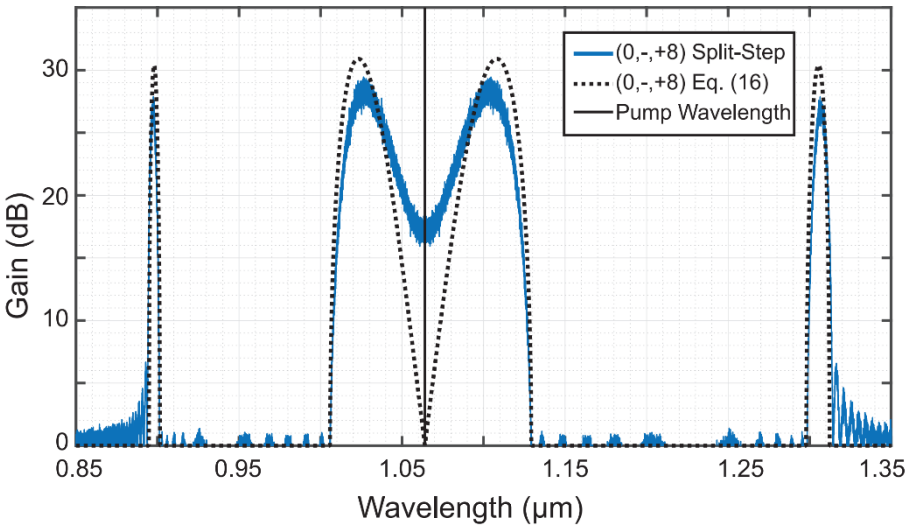

Fig. 3. Simulation results of a pump in the (0,–,+8) spatial mode at 1.064 µm, 1 kW power, and propagating over 3 m. The two pairs of peaks are also in the (0, –,+8) spatial mode, and are characteristic of scalar modulation instability.

We observe that the locations of the new modes are accurately predicted, including the spectral widths, although the gains are slightly overpredicted. The extra oscillations present are attributed to other FWM processes not considered in the analytic derivations. That is, any phase-matched set of frequencies $\beta(\omega_a)+\beta(\omega_b)+\theta(\omega_a)+\theta(\omega_b)=\beta(\omega_c)+\beta(\omega_d)+\theta(\omega_c)+\theta(\omega_d)$ will interact through FWM. The analytic results presented are meant to capture the first-order effects of stably growing modes generated by the pump, i.e. the case where $\omega_a=\omega_b=\omega_0$, where ω_0 is the pump frequency. Furthermore, these and following simulations were performed using a variety of

Optics EXPRESS

Table 1. Dispersion and overlap parameters used for simulations.

	(0,–,+8)	(0,+,+2)	(0,+, –2)
n_{eff}	1.4648	1.4719	1.4714
β_1, s/m	5.043E−9	5.021E−9	5.022E−9
β_2, s^2/m	−4.997E−28	2.088E−26	2.065E−26
β_3, s^3/m	5.327E−41	3.086E−41	2.660E−41
β_4, s^4/m	5.342E−56	2.991E−56	5.989E−56
$Q^{(SPM)}$, V^4/W^2-m^2	2.424E + 15	2.761E + 15	3.285E + 15
$Q^{(XPM)}$, V^4/W^2-m^2	–	3.412E + 15	3.412E + 15

sampling configurations, e.g. z-step size and time-domain sample spacing Δt, to ensure such features are not the result of numerical artifacts.

When considering signals that may be generated in new spatial modes, and the large number of spatial modes that are available in the fiber, it may be desirable to ensure the new signals have smaller bandwidths to prevent spectral overlap and avoid possible interference in signal growth. In Eqs. (16)–(18) we observe that decreasing the pump power will decrease the signal bandwidth, though a longer fiber will be needed to reach the same power levels. To test this, we repeat the prior case but with a 100 W pump and 30 m fiber length. The results are shown in Fig. (4). As predicted, the peak gains remain unchanged while the spectral widths are reduced to $\lesssim$1 nm for the further detuned signals.

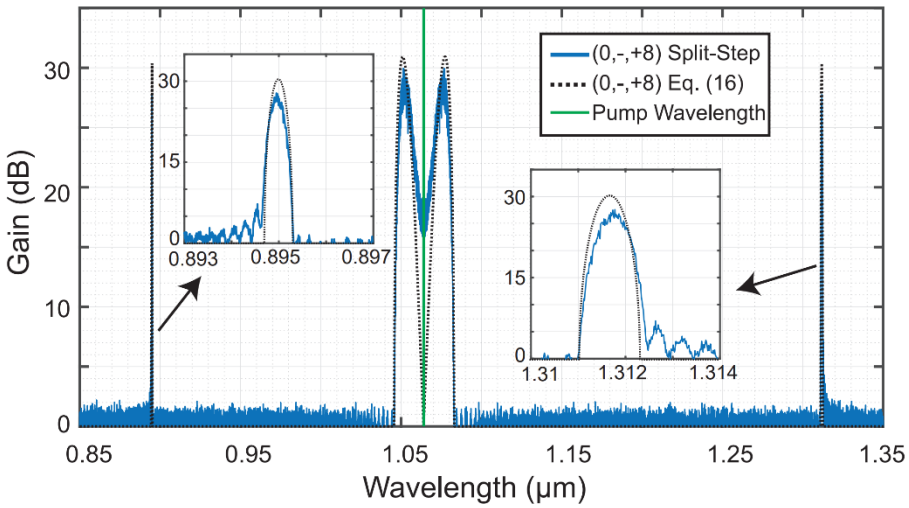

Fig. 4. Simulation results of a pump in the (0, –,+8) spatial mode at 1.064 μm, 100 W power, and propagating over 30 m. The lower power and longer fiber length allows for new signals with narrower bandwidths.

6. Cross-phase modulation instability of the (0,±,+2) spatial modes

We next explore the case of two pumps: one in the (0, –,+2) spatial mode, and the other in the (0,+,+2) spatial mode. Here, again, both pumps consist of 0.8 ns supergaussian pulses centered at 1.064 μm, have 100 W peak power, and propagate 30 m. We consider only new Stokes and anti-Stokes signals in either (0,±,+2) spatial modes. This is equivalent to cross phase modulation

Optics EXPRESS

instability (XPMI). The relevant dispersion and overlap coefficients are provided in the second and third columns of Table 1 (note that, for XPMI, $Q^{(\mathrm{XPM})} = Q^{(\mathrm{FWM3})}$).

The simulation results are presented in Fig. (5). Neither mode has phase-matched SMI processes as the (0,–,+8) spatial mode does; however, there is a XPMI process predicted to occur, based on Eq. (18), with the (0,–,+2) spatial mode at $\lambda_S = 1.1138\,\mu\mathrm{m}$ and the (0,+,+2) spatial mode at $\lambda_A = 1.0185\,\mu\mathrm{m}$. This is consistent with XPMI observed in other fiber types, where the slow mode (higher group index and β_1) is Stokes shifted, while the fast mode (lower group index and β_1) is anti-Stokes shifted [19,29]. Equation (18) also predicts a set of peaks detuned by ~0.1 nm from the pump. These correspond to the first-order approximation to the phase matching condition, $(\beta_{1,S} - \beta_{1,A})\,\Omega = \theta_1 + \theta_2 - \theta_S - \theta_A$, where Ω is the detuning. These signals are not present in the simulation: neither at the end of the 30 m fiber, nor any intermediately sampled distance. Since the derivation of the growth rates provided in Eqs. (16)–(18) effectively assume *distinct* modes which are sufficiently separated in frequency, the very narrow detuning of these modes, and even partial overlap in the gain curves with the pump, may feed other nonlinear processes which suppresses their growth.

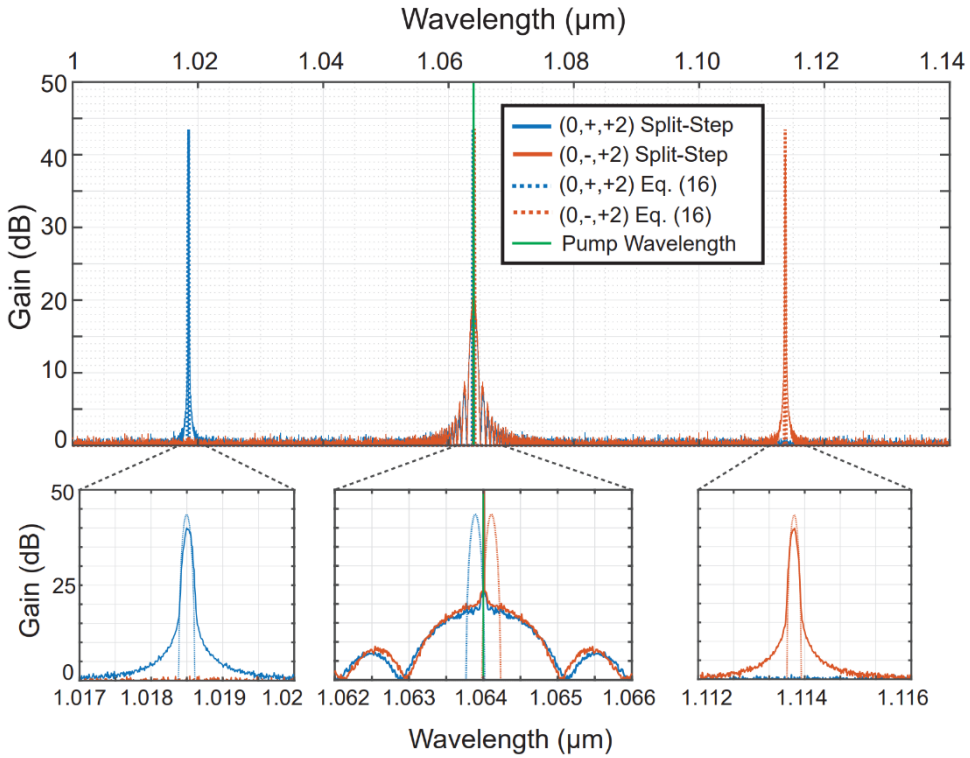

Fig. 5. Simulation results of pumps in the (0,+,+2) and (0,–,+2) spatial modes at 1.064 μm, 100 W power, and propagating over 30 m.

7. Generation of new spatial modes

We now study the generation of spatial modes different than the pump(s), continuing with the case of pumps in the (0,±,+2) spatial modes at 1.064 μm. The FWM overlap integrals, Eqs. (15), are evaluated for all mode permutations and, when they are nonzero, Eqs. (16)–(18) are calculated for the peak growth rates. The results for degenerate and nondegenerate FWM processes are shown in Figs. (6) and (7) respectively. The growth rates are normalized to the pump power and

Optics EXPRESS

are accurate for pumps up to ~1 kW (changes in the Stokes and anti-Stokes frequencies due to nonlinear phase shifts are at most ~1 nm for 1 kW pumps for this test case). The x-axis denotes the Stokes and anti-Stokes modes generated. Note that all generated modes have zero radial order, and thus p is omitted from the mode labels to make the figures more legible. In addition, the last numbers in the labels are the wavelengths in μm. To emphasize how angular momentum evolves between the pump(s) and amplified modes, processes which conserve OAM and SAM independently are marked with blue circles while processes which do not are marked with red x's.

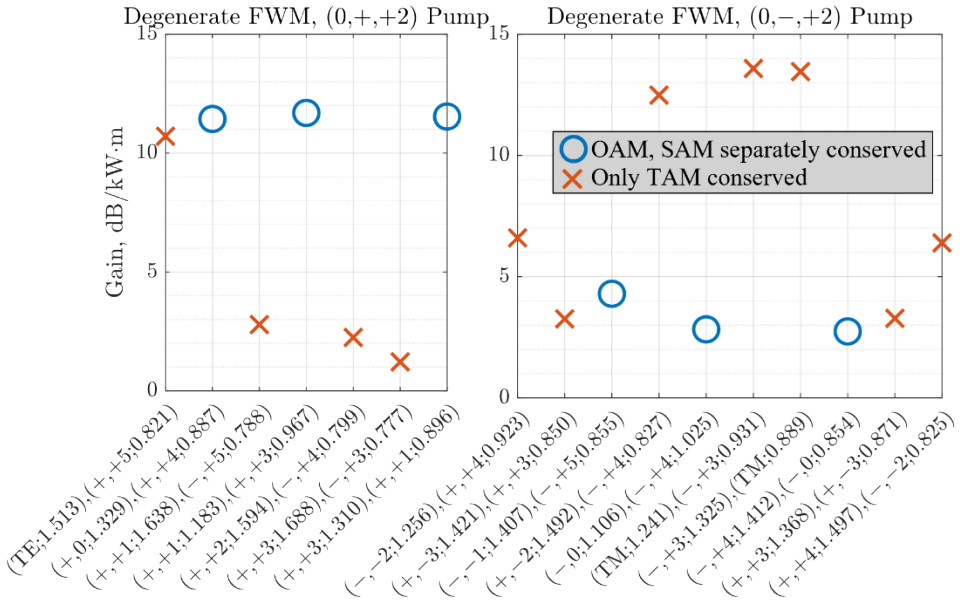

Fig. 6. Modes created by degenerate FWM-based parametric amplification with (0,+,+2) and (0,–,+2) pumps at 1.064 μm. The radial orders p is omitted to keep the figure more legible but are equal to 0. The last numbers in the mode labels are the wavelengths in μm.

Figure (6) (left) provides the growth rates for modes generated by degenerate FWM of the (0,+,+2) pump. Recall that the TAM of an SO mode is quantized by J in Eqs. (1) and (2), i.e. $J = s + \ell$, where s is the dominant spin component and ℓ is the transverse OAM of that dominant spin component, with $J = 0$ for TE and TM modes. Thus, to obtain a nonzero FWM overlap integral, the selection rule $2J_1 = J_A + J_S = +6$ must be satisfied. All of the modes shown satisfy this condition. The differences in gain are due to variations in the mode profiles and thus overlap integral values. An equivalent selection rule of $2J_2 = J_A + J_S = +2$ is enforced for degenerate FWM from the (0, –,+2) pump, which is shown in Fig. (6) (right). Figure (7) shows the growth rates for modes generated by nondegenerate FWM of the two pumps. Here, the selection rule $J_1 + J_2 = J_S + J_A = +4$ is enforced. We note that Raman scattering of the pumps will likely produce a peak at ~1.12 μm, which may mask or disrupt the generation of the modes shown [18].

Under different conditions, such as for a fiber profile with a thicker "ring" section and thus smaller spin-orbit coupling, or when only larger-ℓ modes are involved in the FWM processes, the recessive spin components of the mode profiles can reasonably be discarded, i.e. $\tilde{\mathbf{F}}_{(p,\pm,\ell)}(\mathbf{r}_\perp, \omega_0) \simeq \hat{\boldsymbol{\sigma}}_\pm \tilde{F}_{(p,\pm,\ell)}(r, \omega_0) \exp[i\ell\phi]$. In this case the overlap integrals for FWM-based parametric amplification would enforce independent conservation of SAM and OAM, as has been demonstrated in prior experiments [16,18]. However, for the fiber design and pump configuration considered in this paper, such an approximation is unjustified. For example, one of

Optics EXPRESS

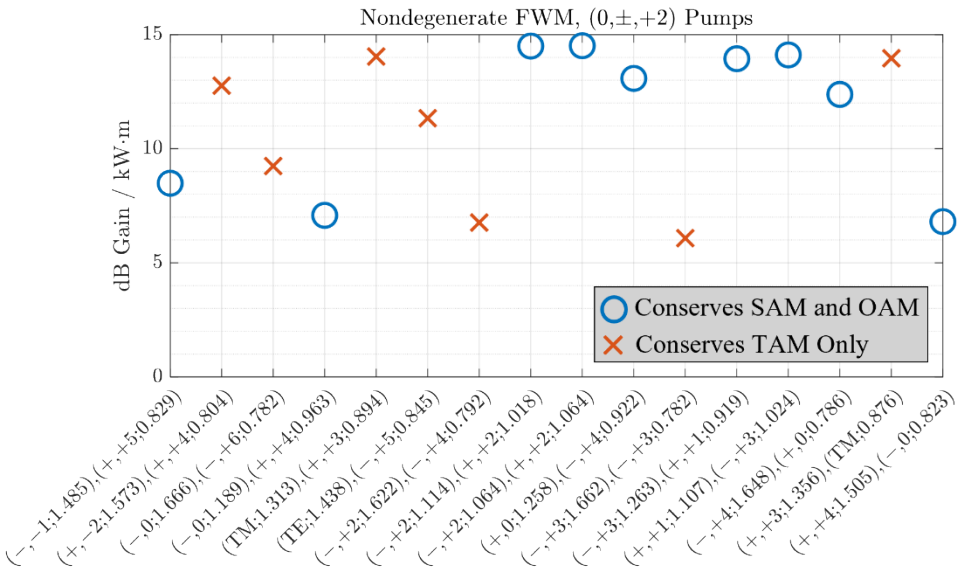

Fig. 7. Modes created by nondegenerate FWM-based parametric amplification with (0,+,+2) and (0, –,+2) pumps at 1.064 µm. The radial orders p is omitted to keep the figure more legible but are equal to 0. The last numbers in the mode labels are the wavelengths in µm.

the most efficient degenerate FWM processes of the (0,–,+2) pump will generate the (0,+,–2) and (0,–,+4) spatial modes at $\lambda_S = 1.492\,\mu m$ and $\lambda_A = 0.827\,\mu m$, respectively. Such a process would be "forbidden" under the reduced case.

8. Conclusion

In this work, we presented a generalized theory of four-wave mixing (FWM)-based parametric amplification for modes in azimuthally symmetric optical fibers. Strictly speaking, the modes in such fibers are characterized by a total angular momentum (TAM) quanta J, where each photon carries $J\hbar$ angular momentum along the propagation axis. Such modes have nonzero LCP and RCP spin components. We showed that this feature translates to selection rules during FWM-based parametric amplification, wherein TAM must be conserved. This is a generalization of prior research [16,18], where the fiber design and mode subset utilized allowed for the modes to be well-approximated as "pure" spin-orbit (SO) modes rather than TAM modes. In such cases the selection rules are more restrictive and correspond to conservation of orbital angular momentum (OAM) and spin angular momentum (SAM) independently.

In addition, we derived growth rates of new modes via degenerate and nondegenerate parametric amplification. Numerical simulations were performed for the cases where the generated Stokes and anti-Stokes modes are in the same spatial mode as the pump(s) – equivalent to scalar and cross-phase modulation instability of the pump beam(s). Our numerical simulations are in good agreement with our theory. We also calculated the growth rates of all new SO modes from a nondegenerate pump configuration and found that processes which "break" the selection rules for independent conservation of SAM and OAM, but are allowed under conservation of TAM, can be significant.

Funding. Office of Naval Research.

Acknowledgments. The authors would like to thank Prof. Siddharth Ramachandran (Boston University) and Dr. Vladimir Markov (Advanced Systems & Technologies, Inc.) for useful discussions and the Office of Naval Research (Q. Saulter) for funding this UMD research.

Optics EXPRESS

Disclosures. The authors declare no conflicts of interest.

Data availability. The data underlying the results presented in this paper are not publicly available at this time but may be obtained from the authors upon reasonable request.

Supplemental document. See Supplement 1 for supporting content.

References

1. L. Allen, M. Beijersbergen, R. Spreeuw, *et al.*, "Orbital angular momentum of light and the transformation of Laguerre-Gaussian laser modes," Phys. Rev. A **45**(11), 8185–8189 (1992).
2. G. Gibson, J. Courtial, and M. Padgett, "Free-space information transfer using light beams carrying orbital angular momentum," Opt. Express **12**(22), 5448–5456 (2004).
3. Y. Ren, Z. Wang, P. Liao, *et al.*, "Experimental characterization of a 400 Gbit/s orbital angular momentum multiplexed free-space optical link over 120 m," Opt. Lett. **41**(3), 622–625 (2016).
4. M. Mirhosseini, M. Malik, Z. Shi, *et al.*, "Efficient separation of the orbital angular momentum eigenstates of light," Nat. Commun. **4**(1), 2781 (2013).
5. D. G. Grier, "A revolution in optical manipulation," Nature **424**(6950), 810–816 (2003).
6. E. Otte and C. Denz, "Optical trapping gets structure: structured light for advanced optical manipulation," Appl. Phys. Rev. **7**(4), 041308 (2020).
7. M. Krenn, M. Malik, M. Erhard, *et al.*, "Orbital angular momentum of photons and the entanglement of Laguerre-Gaussian modes," Phil. Trans. R. Soc. A. **375**(2087), 20150442 (2017).
8. R. Fickler, G. Campbell, B. Buchler, *et al.*, "Quantum entanglement of angular momentum states with quantum numbers up to 10,010," Proc. Natl. Acad. Sci. U.S.A. **113**(48), 13642–13647 (2016).
9. L. Yan, P. Gregg, E. Karimi, *et al.*, "Q-plate enabled spectrally diverse orbital-angular-momentum conversion for stimulated emission depletion microscopy," Optica **2**(10), 900–903 (2015).
10. T. A. Klar, E. Engel, and S. W. Hell, "Breaking Abbe's diffraction resolution limit in fluorescence microscopy with stimulated emission depletion beams of various shapes," Phys. Rev. E **64**(6), 537 (2001).
11. M. P. J. Lavery, F. C. Speirits, S. M. Barnett, *et al.*, "Detection of a spinning object using light's orbital angular momentum," Science **341**(6145), 6145 (2013).
12. N. Cvijestic, G. Milione, E. Ip, *et al.*, "Detecting lateral motion using light's orbital angular momentum," Sci. Rep. **5**(1), 15422 (2015).
13. J. Vieira, R. M. G. M. Trines, E. P. Alves, *et al.*, "Amplification and generation of ultra-intense twisted laser pulses via stimulated Raman scattering," Nat. Commun. **7**(1), 10371 (2016).
14. N. S. Mallick and T. N. Dey, "Four-wave mixing-based orbital angular momentum translation," J. Opt. Soc. Am. B **37**(6), 1857–1864 (2020).
15. P. Gregg, P. Kristensen, A. Rubano, *et al.*, "Enhanced spin orbit interaction of light in highly confining optical fibers for mode division multiplexing," Nat. Commun. **10**(1), 4707 (2019).
16. S. K. Dacha, W. Zhu, A. Agrawal, *et al.*, "Nonlinear rotation of spin-orbit coupled states in hollow ring-core fibers," Opt. Express **30**(11), 18481–18495 (2022).
17. K. Rottwitt, J. G. Koefoed, K. Ingerslev, *et al.*, "Inter-modal Raman amplification of OAM fiber modes," APL Photonics **4**(3), 030802 (2019).
18. X. Liu, E. N. Christensen, K. Rottwitt, *et al.*, "Nonlinear four-wave mixing with enhanced diversity and selectivity via spin and orbital angular momentum conservation," APL Photonics **5**(1), 010802 (2020).
19. S. K. Dacha, H. F. Elder, W. Zhu, *et al.*, "Observation of conjugate OAM mode generation via modulational instability in a hollow ring-core fiber," in *Optica Nonlinear Optics Topical Meeting* 2023, Honolulu (2023).
20. P. Horak and F. Poletti, "Multimode nonlinear fibre optics: theory and applications," *Recent Progress in Optical Fiber Research*, 1–24, (2012).
21. K. Krupa, A. Tonello, B. M. Shalaby, *et al.*, "Spatial beam self-cleaning in multimode fibres," Nature Photon. **11**(4), 237–241 (2017).
22. K. Krupa, A. Tonello, A. Barthélémy, *et al.*, "Multimode nonlinear fiber optics, a spatiotemporal avenue," APL Photonics **4**(11), 110901 (2019).
23. L. G. Wright, Z. Liu, D. A. Nolan, *et al.*, "Self-organized instability in graded-index multimode fibres," Nature Photon. **10**(12), 771–776 (2016).
24. G. Guerra, M. Lonardi, A. Galtarossa, *et al.*, "Analysis of modal coupling due to birefringence and ellipticity in strongly guiding ring-core OAM fibers," Opt. Express **27**(6), 8308–8326 (2019).
25. R. Bhandari, "Nature of the orbital angular momentum (OAM) fields in a multilayered fiber," OSA Continuum **4**(6), 1859–1874 (2021).
26. F. Poletti and P. Horak, "Description of ultrashort pulse propagation in multimode optical fibers," J. Opt. Soc. Am. B **25**(10), 1645–1654 (2008).
27. C. Antonelli, M. Shtaif, and A. Mecozzi, "Modeling of nonlinear propagation in space-division multiplexed fiber-optic transmission," J. Lightwave Technol. **34**(1), 36–54 (2016).
28. G. Agrawal, *Nonlinear Fiber Optics*, 5th ed. (Academic, 2013).
29. A. Kudlinski, A. Bendahmane, D. Labat, *et al.*, "Simultaneous scalar and cross-phase modulation instabilities in highly birefringent photonic crystal fiber," Opt. Express **21**(7), 8437–8443 (2013).
30. L. Li, J. Leng, P. Zhou, *et al.*, "Modulation instability induced by intermodal cross-phase modulation in step-index multimode fiber," Appl. Opt. **58**(16), 4283–4287 (2019).